Article

Synthesis and properties of free-standing monolayer amorphous carbon

Chee-Tat Toh[1,2,10], Hongji Zhang[3,10], Junhao Lin[4,5], Alexander S. Mayorov[2], Yun-Peng Wang[6,7], Carlo M. Orofeo[1], Darim Badur Ferry[1], Henrik Andersen[2], Nurbek Kakenov[2], Zenglong Guo[5], Irfan Haider Abidi[2], Hunter Sims[6], Kazu Suenaga[4,8], Sokrates T. Pantelides[6,9] & Barbaros Özyilmaz[1,2,3]*

Bulk amorphous materials have been studied extensively and are widely used, yet their atomic arrangement remains an open issue. Although they are generally believed to be Zachariasen continuous random networks[1], recent experimental evidence favours the competing crystallite model in the case of amorphous silicon[2–4]. In two-dimensional materials, however, the corresponding questions remain unanswered. Here we report the synthesis, by laser-assisted chemical vapour deposition[5], of centimetre-scale, free-standing, continuous and stable monolayer amorphous carbon, topologically distinct from disordered graphene. Unlike in bulk materials, the structure of monolayer amorphous carbon can be determined by atomic-resolution imaging. Extensive characterization by Raman and X-ray spectroscopy and transmission electron microscopy reveals the complete absence of long-range periodicity and a threefold-coordinated structure with a wide distribution of bond lengths, bond angles, and five-, six-, seven- and eight-member rings. The ring distribution is not a Zachariasen continuous random network, but resembles the competing (nano)crystallite model[6]. We construct a corresponding model that enables density-functional-theory calculations of the properties of monolayer amorphous carbon, in accordance with observations. Direct measurements confirm that it is insulating, with resistivity values similar to those of boron nitride grown by chemical vapour deposition. Free-standing monolayer amorphous carbon is surprisingly stable and deforms to a high breaking strength, without crack propagation from the point of fracture. The excellent physical properties of this stable, free-standing monolayer amorphous carbon could prove useful for permeation and diffusion barriers in applications such as magnetic recording devices and flexible electronics.

Amorphous materials are used in a wide range of applications, but their atomic-scale structure and its effect on properties are far more complex than those of crystalline analogues. In a classic 1932 paper, Zachariasen[1] invoked free-energy arguments to propose that amorphous materials comprise the same bonding units as their crystalline analogues, but these units form continuous random networks (Z-CRNs) instead of periodic structures. A competing model, namely, the existence of crystallites embedded in an otherwise CRN environment, is even older[7] (the crystallite model of amorphous solids is distinct from nanocrystalline materials, as the latter comprise nanoscale grains separated by grain boundaries). In the past few decades, the Z-CRN model has gained wide acceptance, especially for amorphous Si and SiO_2 (a-Si and a-SiO_2), which are viewed as prototypes. The primary experimental

evidence was provided by radial distribution functions, which could be reproduced accurately by model Z-CRNs. More recently, however, experiments that probe beyond pair correlations have found extensive concentrations of nanocrystallites of order 1–2 nm, whereas the corresponding models fit the experimental radial distribution functions just as well as Z-CRN models[2–4]. The inability to image the atomic-scale structure of bulk amorphous materials directly by microscopy means that the debate over CRNs versus crystallites has remained unresolved[8].

For two-dimensional (2D) atomically thin materials, the nature of the amorphous state can in principle be resolved by direct atomic-resolution imaging. Monolayer amorphous carbon (MAC) can be viewed as a prototype amorphous 2D material, an analogue of monolayer crystalline carbon (graphene). Atomic-resolution transmission electron

[1]Department of Physics, National University of Singapore, Singapore, Singapore. [2]Centre for Advanced 2D Materials, National University of Singapore, Singapore, Singapore. [3]Department of Materials Science and Engineering, National University of Singapore, Singapore, Singapore. [4]National Institute of Advanced Industrial Science and Technology, Tsukuba, Japan. [5]Department of Physics, Southern University of Science and Technology, Shenzhen, China. [6]Department of Physics and Astronomy, Vanderbilt University, Nashville, TN, USA. [7]Hunan Key Laboratory for Super-Microstructure and Ultrafast Process, School of Physics and Electronics, Central South University, Changsha, China. [8]Department of Mechanical Engineering, University of Tokyo, Tokyo, Japan. [9]Department of Electrical Engineering and Computer Science, Vanderbilt University, Nashville, TN, USA. [10]These authors contributed equally: Chee-Tat Toh, Hongji Zhang. *e-mail: phyob@nus.edu.sg
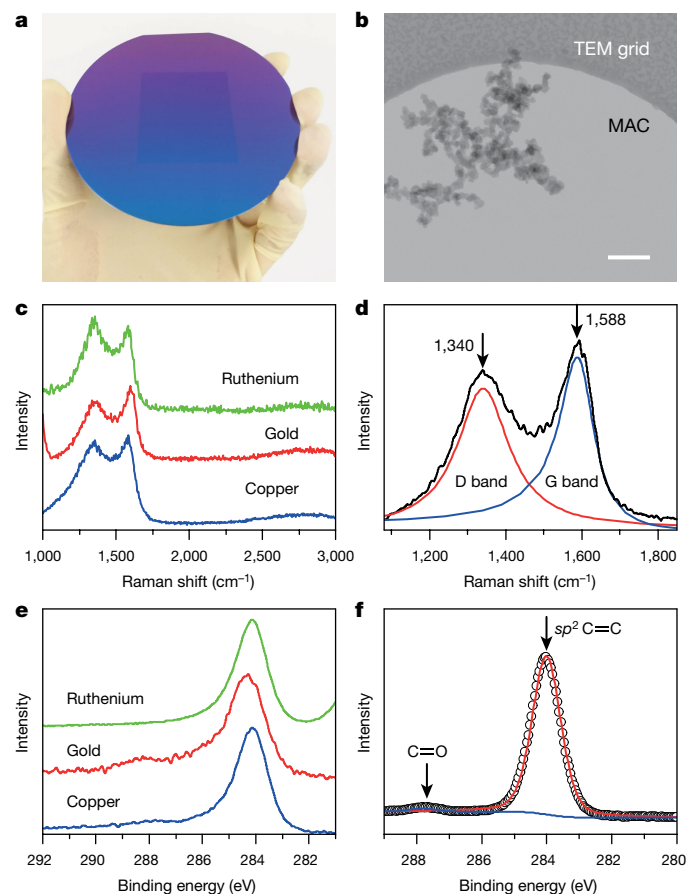
Fig. 1 | Morphology of MAC. a, MAC, 5 × 5 cm², transferred onto a SiO₂/Si wafer. **b**, Scanning electron microscope (SEM) image of MAC suspended on a TEM grid has uniform contrast throughout. Silicon nanoparticles have been intentionally suspended on the MAC to emphasize the presence of the film. Scale bar, 200 nm. **c–f**, Characterization of MAC grown on different substrates. **c**, Raman spectra for MAC grown on copper and gold substrates were measured after transferring to SiO₂. The Raman spectrum for MAC on ruthenium was measured directly on the growth substrate. **d**, Raman spectra for growth on copper, showing the D and G bands with the fitted curve and an I_D/I_G ratio of 0.82. **e**, C 1s XPS spectra measured directly on different growth substrates. **f**, High-resolution C 1s XPS spectra on copper, with the fitted curve showing a single carbon sp^2 peak at 284.0 eV.

microscopy (TEM) has been used to image freestanding graphene monolayers irradiated with TEM electron beams to induce disorder[9,10]. Such monolayers, however, are limited in size, generally inhomogeneous because of carbon loss and, when crystallites are still present, they are not necessarily randomly oriented, as they would be in a truly amorphous material, and can be eliminated by further irradiation. Similarly, radiation of aromatic self-assembled monolayers on substrates produces nanocrystalline graphene with only small amorphous patches[11].

Direct synthesis of MAC samples remains a challenge. Recently, the synthesis of amorphous carbon monolayers on Ge substrates using conventional chemical vapour deposition (CVD) was reported[12]. These samples were grown at high temperatures (>900 °C), resulting in amorphous regions (about 300 nm) that are embedded in a graphene matrix. The reported TEM images lack atomic resolution to establish the structure unambiguously. Instead, the authors concluded in favour of a Z-CRN structure on the basis of the halos in diffraction patterns derived from fast Fourier transform patterns of TEM images of regions 2.5 × 2.5 nm². However, many of the halos exhibit residual six-dot motifs—that is, the existence of crystallites 1–2 nm across cannot be ruled out.

Here we report the synthesis of MAC by a laser-assisted CVD growth process. The self-limiting process leads to a uniform monolayer of several square centimetres in less than 1 minute at substrate temperatures as low as 200 °C. Extensive atomic-resolution TEM characterization shows unambiguously both the complete absence of long-range periodicity and a structure that is consistent with the crystallite model: that is, nanometre-sized, randomly oriented and strained crystallites comprising only six-member rings embedded in a Z-CRN environment. For simplicity, here we discuss representative data on MAC films grown on a copper foil at 250 °C unless otherwise stated. Samples are easily transferred via wet etching after growth. Unlike other CVD-grown 2D materials, MAC is freestanding even on liquid surfaces without the need of a support polymer (Supplementary Video). Figure 1a, b shows that the transferred sample (on a SiO₂/Si wafer and a TEM grid, respectively) is homogeneous and continuous, free from multilayer regions or the wrinkles that are typically observed with the transfer of 2D layers. In addition, MAC is stable and freestanding even when stored under ambient conditions for at least 1 year.

The MAC samples were first characterized by Raman spectroscopy and X-ray photoemission spectroscopy (XPS) measurements. All samples have nearly identical spectra independent of substrate (Fig. 1c, d). The Raman 2D band at approximately 2,680 cm⁻¹, which is pronounced in crystalline graphene, is negligible in the MAC, strongly suggesting the lack of any long-range order[13]. Furthermore, the Raman intensity ratio I_D/I_G = 0.82 (Fig. 1e) indicates an average defect distance[14] of <1 nm. Note that Raman mapping of I_D/I_G shows that MAC is uniform over areas of 50 × 50 μm² (Extended Data Fig. 1). Furthermore, C 1s XPS in Fig. 1f shows that the bonds in MAC are mainly carbon sp^2 (Supplementary Note 1).

Monochromated, aberration-corrected, high-resolution transmission electron microscopy (HRTEM) was used to image the exact arrangement of carbon atoms in MAC. A large-area HRTEM image reveals a connected but distorted structure of five-, six-, seven- and eight-member rings (Fig. 2a). The Fourier transform in the inset of Fig. 2a shows a broad, continuous halo. Figure 2b shows a zoomed-in area of 5 × 5 nm² in which we can clearly see heavily distorted crystallites (green regions) about 1 nm across, embedded in a CRN background that comprises five-, six-, seven- and eight-member rings. As the yellow arrows indicate, the crystallites are oriented randomly. This structure of MAC is consistent over the entire sample (Supplementary Note 2). Thus, MAC is topologically distinct from disordered graphene.

We also evaluated the pair correlation function of neighbouring carbon atoms in MAC samples (Fig. 2e) and a graphene reference (Supplementary Note 3), a crucial property in deciding whether a material is amorphous. Graphene peaks disappear or are highly broadened in the MAC pair correlation function after the second nearest neighbours, confirming the loss of long-range periodic order. The bond lengths and angles for graphene are centred at 1.4 Å and 120°, respectively, with small variation arising from image aberration and algorithmic error. In contrast, MAC has much broader variation, 0.9–1.8 Å and 90–150° for the in-plane projections of bond lengths and bond angles, respectively (Fig. 2f, g). This feature is surprising because the theoretical breaking strain at 25–30% for crystalline graphene occurs with deformations[15] at just under 1.6 Å and 135°, so one would expect freestanding MAC to be unstable and subject to collapse. On the other hand, such a wide spread in the bond angle distribution is expected for a random 2D amorphous network, similar to the O–Si–O bonds modelled in a silica bilayer on ruthenium[16]. Moreover, each carbon atom is three-fold coordinated, consistent with the sp^2 bonding concluded from the XPS data.

Furthermore, the strained crystallites are fundamentally different from nanocrystalline graphene domains because they are separated not by atomically sharp grain boundaries, but by CRN regions that are at least three carbon atoms wide (Fig. 2h, i). Selective-area electron diffraction (SAED) patterns show a characteristic diffuse halo (Fig. 2j) that confirms the amorphous nature of MAC, in contrast to the sharp first- and second-order diffraction rings for nanocrystalline graphene
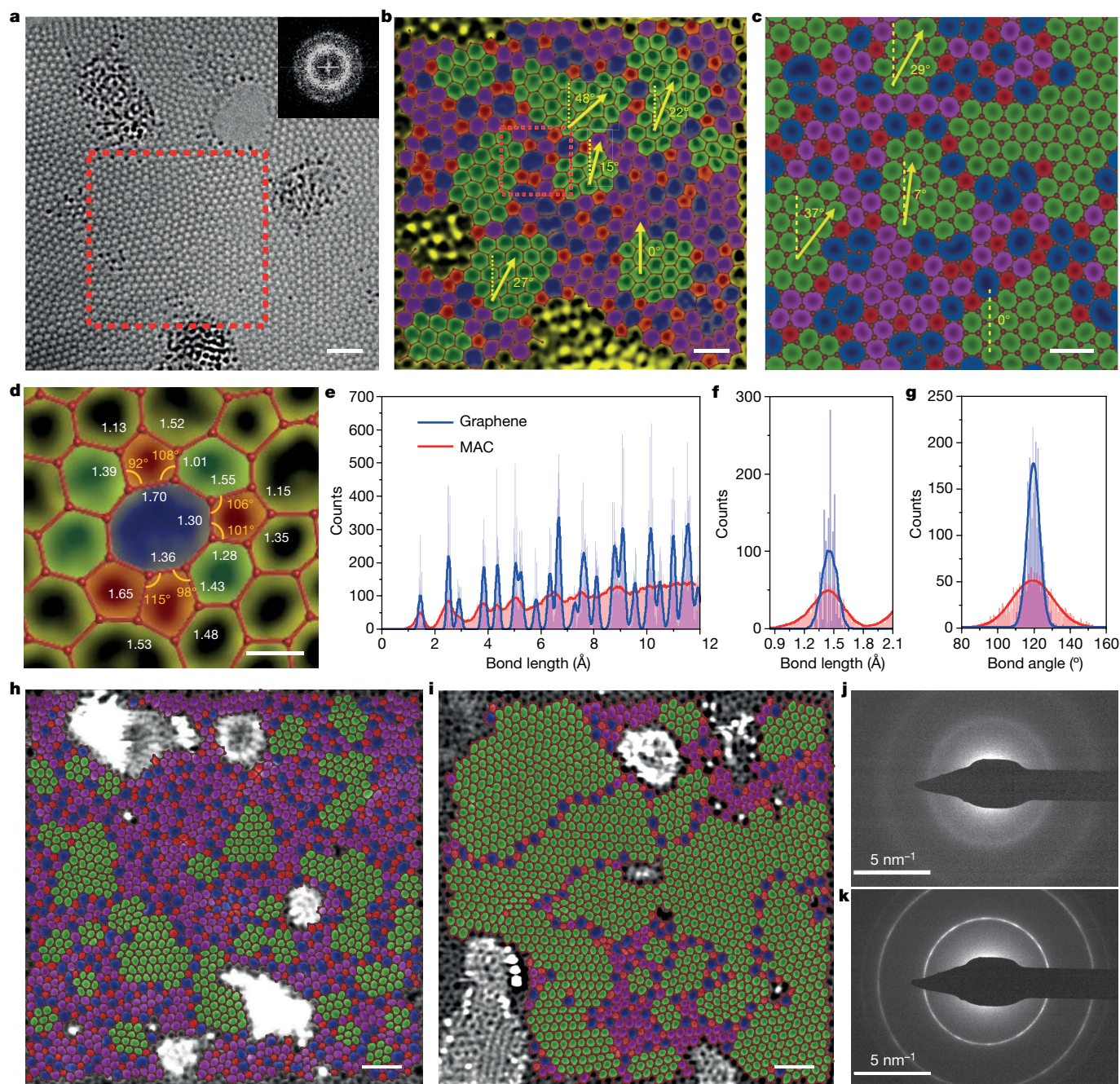
Fig. 2 | Atomic structure of MAC from TEM. a, Monochromated HRTEM image of MAC, 10×10 nm², and the corresponding Fourier transform of the selected region (inset). **b**, Large-scale atom-by-atom mapping of the selected region, 5×5 nm², in **a**. The image contrast is inverted and false-coloured for better visibility. Colour overlay is added for identification of pentagons (red), heptagons/octagons (blue) and strained hexagons (purple for individual hexagons; green for crystallite regions) that are omnipresent. Crystallites (regions of green hexagons) separate the regions with non-hexagons. Crystallites are defined to consist of at least a hexagonal ring surrounded by six hexagonal rings. Angular orientation of the hexagons changes across the image, as indicated by yellow arrows and the offset angle to the vertical. **c**, Theoretical model created as described in Extended Data Fig. 7, replicating the MAC features in **b** and displayed with same colour coding. **d**, Zoom-in region highlighted by the red square in **b**. The bond lengths (in ångström) and bond angles of each pentagon are precisely measured. **e**, Pair correlation function calculated by mapping the coordinates of each carbon atom in **b**. Graphene imaged under similar conditions with the same mapping algorithm is shown as a reference. **f**, Statistical histogram of the distribution of bond length to the first neighbouring atoms for MAC and graphene. **g**, Statistical histogram of the bond angle distribution for MAC and graphene. **h**, **i**, Comparison of scanning transmission electron microscopy (STEM) imaging for MAC (**h**) and nanocrystalline graphene (**i**), with false-colour overlay. Original images shown in Supplementary Note 3. **j**, **k**, SAED patterns over a 3-μm-diameter region: for the MAC sample shown in **h** (**j**) and for the nanocrystalline graphene sample shown in **i** (**k**). Scale bars, 1 nm (**a**), 0.5 nm (**b**, **c**), 0.2 nm (**d**), 1 nm (**h**, **i**) and 5 nm⁻¹ (**j**, **k**).

(Fig. 2k). Dark-field TEM also reveals this, with only nanocrystalline graphene showing crystallinity (Extended Data Fig. 2 and Supplementary Note 3). To summarize, the direct imaging of the atomic structure clearly shows the amorphous nature of MAC to be (nano)crystallite, not Z-CRN.

The interlayer spacing of multilayer MAC was measured by atomic force microscopy (AFM) of overlapping MAC layers prepared by multiple wet transfers on a SiO₂/Si substrate. The spacing was found to be approximately 0.6 nm (Fig. 3b, Extended Data Fig. 3). This interlayer spacing is almost twice as large as that of graphene, similar to
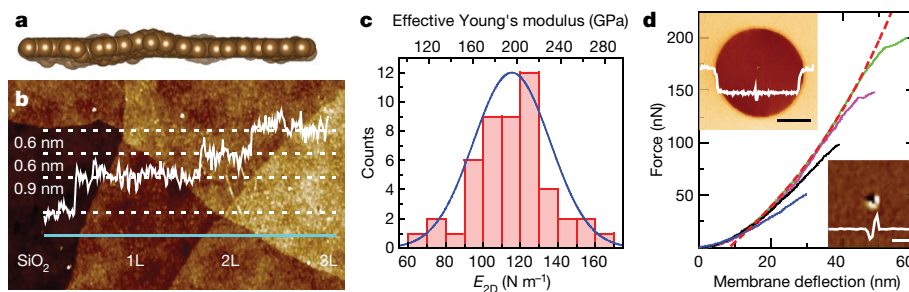
Fig. 3 | Mechanical properties of MAC. a, Side view of the model MAC shown from above in Fig. 2c, showing out-of-plane structural relaxation. **b**, AFM topography of one to three layers of MAC on SiO$_2$/Si. The cyan solid line indicates the line-scan position for the overlaid height profile. Image width, 3 μm. **c**, Histogram of the 2D elastic stiffness (E_{2D}) of 49 suspended MAC membranes with applied force of 100 nN, with an average of $E_{2D} = 115 \pm 21$ N m^{-1}. **d**, Selected force–displacement curves from multiple indentations with increasing force applied in 25-nN steps. Fitting to the linear elastic deformation expression is indicated by the dashed red line. Top inset, AFM scan of MAC suspended on a 2.5-μm-diameter well. The white line is the height profile along the centre with a 10.0-nm adhesion depth to the well wall. Bottom inset, close-up of collapsed MAC (the white line is the height profile along the centre) after repeated indentations at 200 nN. Scale bars, 1 μm (**d**, top inset) and 100 nm (**d**, bottom inset).

phosphorene's 0.6 nm, and consistent with the out-of-plane buckling caused by Stone–Wales defects[17]. AFM indentation experiments on suspended MAC membranes were used to determine the impact of structural buckling on its mechanical properties. The distribution of 2D elastic stiffness (E_{2D}) obtained by force–deflection measurements to 100 nN is centred at $E_{2D} = 115$ N m^{-1} (Fig. 3c). We observed an increasing slope (hence stiffness) of the force–displacement curves with consecutive indentations of increasing force (Fig. 3d). Hence, MAC undergoes plastic deformation with applied force. Furthermore, we obtain a breaking strength of 22 N m^{-1}, more than half the strength of single-crystal graphene[18]. We note that indentation rupture is restricted and does not propagate (Fig. 3c), in contrast to similar experiments with crystalline graphene that result in catastrophic failure by rapid crack propagation[18] (Supplementary Note 4).
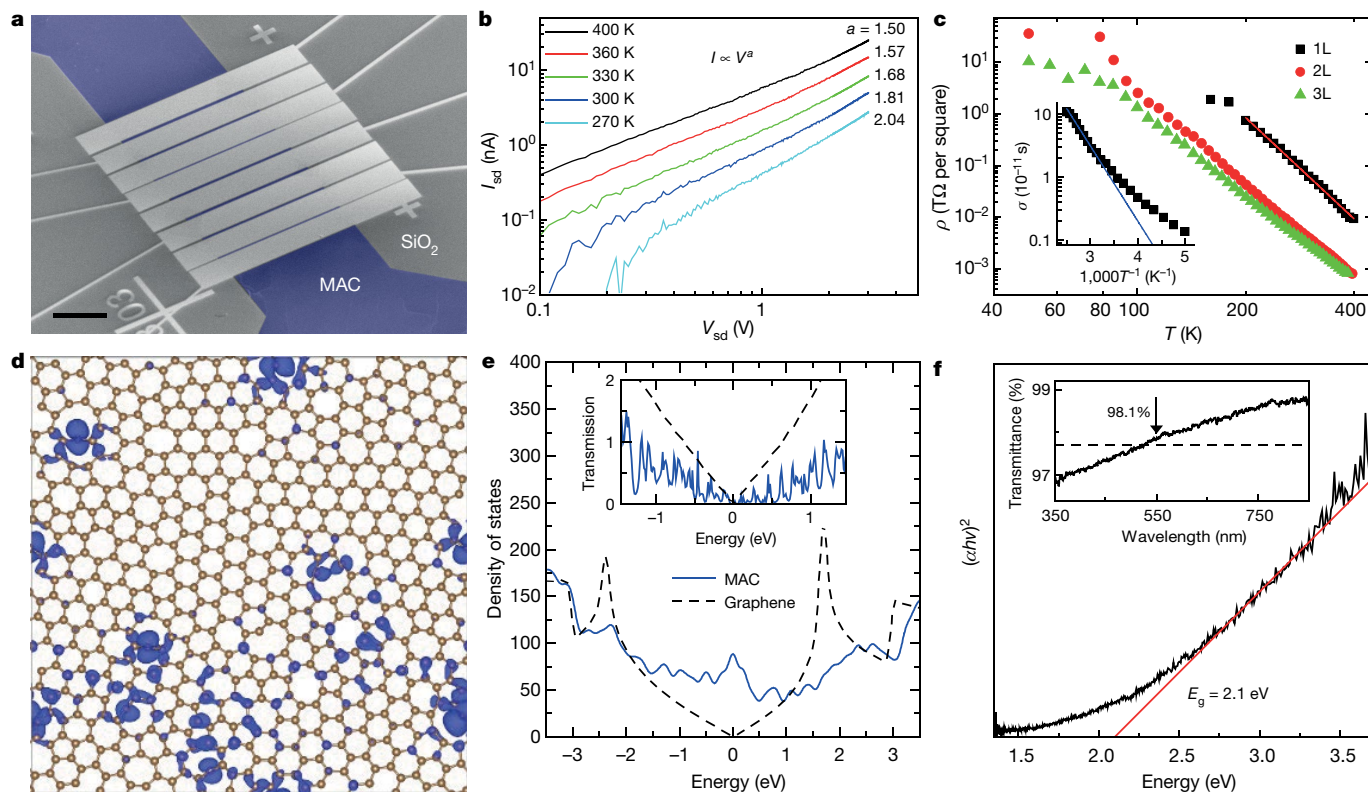

Fig. 4 | Insulating properties of MAC. a, False-colour SEM image of the two-terminal device with a channel width of 500 nm to 1 μm and electrodes 50 μm long. Scale bar, 20 μm. **b**, Nonlinear I–V curves measured at five different temperatures (Extended Data Fig. 4). **c**, Resistivity for samples with different layer (L) numbers as a function of temperature. The red line is the linear best fit with offset α and slope N equal to $10^{(26.9 \pm 0.05)}$ and -6.5 ± 0.05, respectively. Leakage current from SiO$_2$/Si prevents lower-temperature measurements. Inset, the Arrhenius plot gives an activation energy of 235 meV. **d**, Top view of the model MAC overlaid by the modulus square of the lowest unoccupied wavefunction. **e**, The density of states of the model MAC (solid blue line) shows a peak at the Fermi energy (zero energy on the plot) compared with that of graphene (dashed black line). Inset, phase-coherent electronic transmission through the model MAC (solid blue line) compared with that through graphene (dashed black line). **f**, Tauc plot calculated using an absorption coefficient α and photon energy $h\nu$ (h, Planck constant; ν, frequency) to determine the optical bandgap in amorphous materials, with extrapolation of the linear region (red line) estimating an optical bandgap of 2.1 eV. Inset, optical transmittance of MAC on CaF$_2$ substrate. The dashed line indicates pristine graphene absorption at 2.3%.

Next, we discuss source–drain bias-dependent electronic transport measurements (I–V) as a function of temperature and layer number (see also Extended Data Fig. 4). In all samples that we observed, $I = V^{\alpha}$, where $\alpha \approx 2$ (Fig. 4b) and the sheet resistance values are of order 100 GΩ at room temperature, similar to CVD boron nitride[19]. These sheet resistance values are high for a 2D material and are up to about 10 orders of magnitude larger than for graphene. Furthermore, the large activation energy of 235 meV (obtained from the Arrhenius plot in Fig. 4c) is similar to what has been observed in CVD boron nitride (193 meV)[20]. On the other hand, the temperature dependence of the resistivity ρ exhibits (Fig. 4c) a power-law dependence, $\rho = \alpha T^{N}$, instead of the expected Mott law ($\rho \propto e^{(T/T_0)^{-\gamma}}$, where α, N and γ are fitting factors) for variable-range hopping (Extended Data Fig. 5). In addition, we observe that the temperature dependence of all I–V curves collapses to a single curve, indicating an apparent power-law dependence (Extended Data Fig. 6). The two results together suggest that charge transport in MAC is unique in 2D and mimics that in disordered quasi-one-dimensional systems, known as rare-chain hopping[21,22].

A periodically repeatable structural model of MAC was constructed to resemble the observed structure in Fig. 2b, with similar distribution of ring size and similar randomly oriented crystallites embedded in a Z-CRN network (Fig. 2c; see Extended Data Fig. 7 for the construction process). Relaxation of the structure using density-functional-theory calculations produced buckling in the non-hexagon regions (Fig. 3a), as is known to occur at Stone–Wales defects in graphene[17]. We also constructed bilayer MAC by stacking the model structures at different relative displacements and minimized the total energy with respect to interlayer spacing. We obtained interlayer spacings ranging from 0.55 nm to 0.62 nm, in agreement with the measured interlayer spacings discussed above. Quantum molecular dynamics simulations of the structure at 300 K reveal that the MAC is stable and undergoes out-of-plane distortions in the entire structure in the form of long-wavelength flexural phonons, similar to those in graphene[23].

The experimental results described above are in good agreement with electronic-structure and quantum transport calculations performed with the MAC model described earlier (Fig. 2c). In Fig. 4e, we show the calculated MAC density of states (DOS) and compare it with that of crystalline graphene. It is clear that the V-shaped DOS of crystalline graphene around the Dirac point is no longer present. Instead, the DOS shows a relatively broad peak at the nominal Fermi energy, suggesting an increase of localized states[24]. In Fig. 4d, we plot the wavefunction (shown in blue) of a state within this peak, showing significant localization on non-hexagon rings that are separated by crystallites (Extended Data Fig. 8). The calculated transmission coefficient in the region around the Fermi energy, shown in the inset in Fig. 4e, approaches zero despite the high DOS, which explains the highly resistive charge transport.

To identify the effective bandgap of MAC, we measured its optical properties. The optical transmittance of MAC is 98.1% at 550 nm and increases towards 99% in the infrared (Fig. 4f). Clearly, graphene's 2.3% minimum absorption defined by the fine structure constant is no longer applicable. More importantly, a Tauc plot gives an optical bandgap of 2.1 eV with a long tail towards lower energies, which is reminiscent of 'tail states' in 3D amorphous silicon[25]. We also observed photoluminescence from MAC with a pronounced peak at 2.04 eV, which is not seen in graphene owing to the absence of a bandgap. Charge localization could be responsible for both the optical gap and the observation of photoluminescence, similar to insulating sp^3 amorphous carbon thin films with charge localization at isolated sp^2 clusters[26]. Finally, ellipsometry confirmed a bandgap at 2.1 eV and a corresponding relative permittivity of about 11 (Extended Data Fig. 9).

In summary, we have demonstrated a method for the growth of a stable amorphous material in the 2D limit, by producing large-area, freestanding monolayers of sp^2-bonded amorphous carbon films. We have furthermore demonstrated that the ring distribution is not a

Z-CRN but resembles the competing crystallite model. Overall, so far, there exists no solid evidence for the formation of homogeneous, stable, freestanding Z-CRN monolayers, although their existence cannot be ruled out. Finally, stable MAC films directly grown on a wide range of surfaces at low temperatures are likely to be useful for a wide range of applications, including anti-corrosion barriers for heat-assisted magnetic recording on magnetic hard disks, and for current collectors and electrodes in batteries and supercapacitors. The possibility of engineering a distribution of carbon ring sizes also makes MAC attractive for proton transport membranes.

Online content

Any methods, additional references, Nature Research reporting summaries, source data, extended data, supplementary information, acknowledgements, peer review information; details of author contributions and competing interests; and statements of data and code availability are available at https://doi.org/10.1038/s41586-019-1871-2.

1. Zachariasen, W. H. The atomic arrangement in glass. *J. Am. Chem. Soc.* **54**, 3841–3851 (1932).
2. Voyles, P. M. & Abelson, J. R. Medium-range order in amorphous silicon measured by fluctuation electron microscopy. *Sol. Energy Mater. Sol. Cells* **78**, 85–113 (2003).
3. Gibson, J. M., Treacy, M. M. J., Sun, T. & Zaluzec, N. J. Substantial crystalline topology in amorphous silicon. *Phys. Rev. Lett.* **105**, 125504 (2010).
4. Treacy, M. M. J. & Borisenko, K. B. The local structure of amorphous silicon. *Science* **335**, 950–953 (2012).
5. Herman, I. P. Laser-assisted deposition of thin films from gas-phase and surface-adsorbed molecules. *Chem. Rev.* **89**, 1323–1357 (1989).
6. Wright, A. C. Neutron scattering from vitreous silica. V. The structure of vitreous silica: what have we learned from 60 years of diffraction studies? *J. Non-Cryst. Solids* **179**, 84–115 (1994).
7. Wright, A. C. The great crystallite versus random network controversy: a personal perspective. *Int. J. Appl. Glass Sci.* **5**, 31–56 (2014).
8. Roorda, S. & Lewis, L. J. Comment on "The Local Structure of Amorphous Silicon". *Science* **338**, 1539 (2012).
9. Eder, F. R., Kotakoski, J., Kaiser, U. & Meyer, J. C. A journey from order to disorder—atom by atom transformation from graphene to a 2D carbon glass. *Sci. Rep.* **4**, 4060 (2014).
10. Kotakoski, J., Krasheninnikov, A. V., Kaiser, U. & Meyer, J. C. From point defects in graphene to two-dimensional amorphous carbon. *Phys. Rev. Lett.* **106**, 105505 (2011).
11. Turchanin, A. et al. Conversion of self-assembled monolayers into nanocrystalline graphene: structure and electric transport. *ACS Nano* **5**, 3896–3904 (2011).
12. Joo, W.-J. et al. Realization of continuous Zachariasen carbon monolayer. *Sci. Adv.* **3**, e1601821 (2017).
13. Zandiatashbar, A. et al. Effect of defects on the intrinsic strength and stiffness of graphene. *Nat. Commun.* **5**, 3186 (2014).
14. Araujo, P. T., Terrones, M. & Dresselhaus, M. S. Defects and impurities in graphene-like materials. *Mater. Today* **15**, 98–109 (2012).
15. Zhang, C., Hao, X.-L., Wang, C.-X., Wei, N. & Rabczuk, T. Thermal conductivity of graphene nanoribbons under shear deformation: a molecular dynamics simulation. *Sci. Rep.* **7**, 41398 (2017).
16. Lichtenstein, L. et al. The atomic structure of a metal-supported vitreous thin silica film. *Angew. Chem. Int. Ed.* **51**, 404–407 (2012).
17. Lusk, M. T. & Carr, L. D. Nanoengineering defect structures on graphene. *Phys. Rev. Lett.* **100**, 175503 (2008).
18. Lee, C., Wei, X., Kysar, J. W. & Hone, J. Measurement of the elastic properties and intrinsic strength of monolayer graphene. *Science* **321**, 385–388 (2008).
19. Mahvash, F., Paradis, E., Drouin, D., Szkopek, T. & Siaj, M. Space-charge limited transport in large-area monolayer hexagonal boron nitride. *Nano Lett.* **15**, 2263–2268 (2015).
20. Kim, D. Y., Jeong, H., Kim, J., Han, N. & Kim, J. K. Defect-mediated in-plane electrical conduction in few-layer sp^2-hybridized boron nitrides. *ACS Appl. Mater. Interfaces* **10**, 17287–17294 (2018).
21. Rodin, A. S. & Fogler, M. M. Apparent power-law behavior of conductance in disordered quasi-one-dimensional systems. *Phys. Rev. Lett.* **105**, 106801 (2010).
22. Rodin, A. S. & Fogler, M. M. Hopping transport in systems of finite thickness or length. *Phys. Rev. B* **84**, 125447 (2011).
23. Morozov, S. V. et al. Giant intrinsic carrier mobilities in graphene and its bilayer. *Phys. Rev. Lett.* **100**, 016602 (2008).
24. Kapko, V., Drabold, D. A. & Thorpe, M. F. Electronic structure of a realistic model of amorphous graphene. *Phys. Status Solidi B* **247**, 1197–1200 (2010).
25. Tauc, J. Optical properties and electronic structure of amorphous Ge and Si. *Mater. Res. Bull.* **3**, 37–46 (1968).
26. Rusli Amaratunga, G. A. J. & Silva, S. R. P. Photoluminescence in amorphous carbon thin films and its relation to the microscopic properties. *Thin Solid Films* **270**, 160–164 (1995).

Article

Methods

MAC synthesis

MAC was synthesized by laser-assisted chemical vapour deposition (LCVD) process with krypton fluoride (KrF) pulsed laser (λ = 248 nm, Coherent Inc.). Copper foils (35 μm thick) were cleaned by sonication in acetone and isopropyl, followed by 30 min annealing in H_2 at 1,010 °C in a quartz tube furnace. Sputtered Au and Ru substrates were used without prior annealing. The growth substrates were transferred into the LCVD vacuum chamber and mounted on the titanium stage. The chamber was evacuated to base pressure of 10^{-6} mbar. CH_4 was introduced into the chamber to 10^{-2} mbar pressure. The substrate was exposed to a plasma (350 kHz pulsed d.c. generator at 20 W) and pulsed laser (40 mJ cm^{-2}, 50 Hz) over a 5-cm^2 area, for complete film formation under 1 min. To obtain larger area coverage, the stage was rastered with constant motion relative to the laser spot. Substrate temperatures were monitored by an infrared thermal sensor (Optis CTlaser 3MH$_2$-CF$_4$). Growth durations ranged from 1 min to 10 min, with temperatures due to laser heating between 200 °C and 500 °C; MAC growth was of similar quality. Substrate temperatures can be further controlled by a stage heater, for nanocrystalline graphene grown between 500 °C and 650 °C, and polycrystalline graphene grown at >650 °C. Although MAC synthesized on both sides of the copper foil has a similar amorphous quality, MAC from the underside (facing away from the laser) was used for detailed characterizations.

MAC sample preparation

MAC from the top side of the substrate was first removed by 5 min of 50-W Ar plasma. The Cu foil was wet etched in 0.7 wt% ammonium persulfate solution ($(NH_4)_2S_2O_8$), by floating the growth substrate on the solution, with MAC facing up without a polymer support. It was transferred to deionized water for 2 h twice, using a rigid substrate, to rinse the interface (that is, it was twice transferred and rinsed) before scooping onto the desired substrate (SiO_2/Si wafers or PELCO holey SiN TEM grids with 2.5-μm pores). For transfer of MAC to SiO_2/Si substrate with holes for the indentation experiment, spin-coated PMMA (495 PMMA, A4, 4% in anisole, 4,000 rpm) was required as a polymer support during the transfer process. Spin-coated samples were baked on a hotplate at 180 °C for 2 min after spin-coating, and the same transfer steps were performed. Suspended MAC was dried supercritically from acetone in a critical point dryer system. The samples were annealed in 5% H_2 in Ar gas for 5 h to remove any organic residues.

Sample characterization

SEM images were acquired using a FEI Verios 460 field emission scanning microscope. Raman spectroscopy was measured by ALPHA 300 R from WITEC (532-nm excitation laser, 1-μm-diameter circular laser spot). Raman spectra for MAC grown on Cu and Au were measured after transfer to SiO_2 substrate, whereas the Raman spectrum was obtained directly on the Ru substrate. XPS spectra were measured using UHV Vacuum Generators ESCALAB Mk2 system with Omicron 7-Channeltron analyser, directly on the growth substrate for Cu, Au and Ru. The high-resolution angle-resolved XPS spectrum on Cu was measured using the Singapore Synchrotron Light Source at the National University of Singapore, with an Omicron EA 125 hemisphere energy analyser. XPS C 1s peaks were fitted after a Shirley background subtraction using XPSPEAK software with a 30% of Lorentzian–Gaussian ratio. The fitted data show a single sp^2-hybridized carbon peak with full-width half-maximum of 1.0. MAC was transferred to a calcium difluoride substrate for optical measurements. The ultraviolet–visible absorbance was recorded at room temperature on a SHIMADZU UV-3600 spectrophotometer. Photoluminescence measurements were performed with an NT-MDT NTEGRA SPECTRA confocal Raman microscope in backscattering geometry. We used the excitation laser at 473 nm and a 100× objective lens with numerical aperture of 0.6 to focus to a spot size of approximately 1.5 μm. The laser power density was kept below 1 kW cm^{-2} to avoid heating effects. The photoluminescence signal was detected with a charge-coupled device array operating at −80 °C. Optical measurements were performed in high vacuum (10^{-5} mbar).

Transmission electron microscopy

The dark-field TEM (DF-TEM) imaging was conducted in an FEI Tecnai F30 microscope operating at 80 kV. DF-TEM images were recorded using the diffraction rings selected by the objective aperture, with a recording time of 120 s for each image. MAC HRTEM imaging was performed on a non-commercialized JEOL ARM60 microscope equipped with a Schottky field emission gun, a JEOL double Wien filter monochromator, double delta correctors and a Gatan OneView camera with high stability. A slit of 2.8 μm was used for energy filtering, enabling a spatial resolution of 1.1 Å with a beam current of about 20 pA. The microscope was operated at 60 kV. The STEM imaging was done in a JEOL 2100F with delta probe corrector, which corrects the aberration up to fifth order, resulting in a probe size of 1.0 Å. The imaging was conducted at an acceleration voltage of 60 kV. The convergent angle for illumination was about 35 mrad, with a collection detector angle ranging from 45 mrad to 200 mrad. A JEOL heating-holder was used in all experiments to heat the sample up to 700 °C during imaging. The pair correlation function and bond angle distribution were calculated from the coordinates of the carbon atoms determined in the HRTEM and STEM images by a home-built atom-finding algorithm.

Computational method

The theoretical model for the crystallite MAC was constructed using the kinetic Monte Carlo method[27]. The simulation starts with a supercell, 40×40 Å^2, containing 610 carbon atoms randomly placed in the x–y plane. The density of carbon atoms is the same as in crystalline graphene. The supercell is then relaxed using a conjugated gradient algorithm. The interatom interactions are described using the adaptive intermolecular reactive empirical bond-order (AIREBO) potential by Stuart[28] as implemented in the LAMMPS molecular dynamics program[29]. Starting from the initial configuration, kinetic Monte Carlo is used for annealing. In each Monte Carlo iteration, one Stone–Wales transformation is performed to the current configuration: that is, one randomly chosen bonded carbon–carbon pair is rotated by 90° in the x–y plane. The probability to accept the new relaxed structure is min $\{1, \exp((E_{old} - E_{new})/k_B T)\}$, where E_{old} is the energy of the current configuration, E_{new} is the energy of the new configuration after relaxation, and $k_B T$ is selected to be 0.5 eV (k_B, Boltzmann constant). We perform more than 60,000 iterations and generate 1,560 distinct configurations. We select the configuration at the 20,000th iteration as the theoretical model for its similarity with the experimental HRTEM image (Extended Data Fig. 7). The electronic structure is calculated using density functional theory in the generalized gradient approximation[30] as implemented in the VASP software[31]. The coherent electronic transmission probability is calculated using the Transiesta programme.

Mechanical characterization

AFM topography was measured by tapping mode using a Bruker AFM. This was also used for indentation experiments. MAC was suspended on wells with diameter of 1–2.5 μm. Force–displacement curves were obtained from indentation experiments performed at the centre of the suspended membranes using single-crystal diamond probes with 8-nm diamond tips (spring constant of 1–5 N m^{-1}) attached to silicon cantilevers (K-TEK nanotechnology). The applied force was then increased until fracture to obtain the breaking strength of MAC. The 2D elastic constant of MAC was calculated by fitting the force–displacement results using the equation for force[32]

$$F = \frac{2\pi\sigma\delta}{\ln(a/r)} + \frac{Eq^3\delta^3}{a^2} \tag{1}$$

where a and r are the radius of the suspended membrane and the AFM tip, respectively. σ, δ and E are the 2D pre-tension, deflection and 2D effective Young's modulus of the membrane, respectively, and q (~1.02) is a function of Poisson's ratio (taken as 0.165).

The breaking strength corresponding to a breaking force F_b was then calculated as

$$\sigma^{2D} = \left(\frac{F_b E}{4\pi r}\right)^{1/2} \tag{2}$$

Electronic transport characterization

Multi-terminal devices of one-, two- and three-layer-thick MAC were fabricated on a Si/SiO$_2$ wafer using the standard microfabrication procedures of electron beam lithography. Oxygen plasma was first used to pattern MAC to fixed width of 50 μm. Devices were created with channel length between 200 nm and 1,000 nm. The width-to-length ratio ranged from 50 to 250. The geometry of each sample is shown in Supplementary Table. After the second step of lithography, a set of Co electrodes (35 nm thick) were deposited in an ultrahigh vacuum system by an electron-beam evaporator at the deposition pressure of 1×10^{-8} torr. Contacts 10 μm wide were made to reduce the contact resistance (Fig. 4a). Electrical measurements were carried out in the d.c. regime using two Keithley 2400 Sourcemeters for source–drain and gate voltages, which allows applying a voltage and measure the current simultaneously. The gate leakage was lower than 1 nA at room temperature and below 25 pA at 150 K. All measurements, for 2D amorphous carbon films, were performed in helium-free cryostats and in vacuum better than 10^{-5} mbar to ensure reproducible measurement conditions. Resistivity measurements are performed at source-drain voltage of 1 V. Resistance was extracted from the I–V characteristic using a polynomial fit and taken at the first derivative at zero voltage.

Data availability

The data that support the findings of this study are available from the corresponding author upon reasonable request.

Code availability

The code used in this study is available upon request from the corresponding author.

27. Zhuang, J., Zhao, R., Dong, J., Yan, T. & Ding, F. Evolution of domains and grain boundaries in graphene: a kinetic Monte Carlo simulation. *Phys. Chem. Chem. Phys.* **18**, 2932–2939 (2016).
28. Stuart, S. J., Tutein, A. B. & Harrison, J. A. A reactive potential for hydrocarbons with intermolecular interactions. *J. Chem. Phys.* **112**, 6472–6486 (2000).
29. Plimpton, S. Fast parallel algorithms for short-range molecular dynamics. *J. Comput. Phys.* **117**, 1–19 (1995).
30. Perdew, J. P., Burke, K. & Ernzerhof, M. Generalized gradient approximation made simple. *Phys. Rev. Lett.* **77**, 3865–3868 (1996).
31. Kresse, G. & Furthmüller, J. Efficient iterative schemes for ab initio total-energy calculations using a plane-wave basis set. *Phys. Rev. B* **54**, 11169–11186 (1996).
32. Ruiz-Vargas, C. S. et al. Softened elastic response and unzipping in chemical vapor deposition graphene membranes. *Nano Lett.* **11**, 2259–2263 (2011).

Extended Data Fig. 1 | Optical image and Raman mapping of MAC film transferred on Si/SiO2 substrate. a, MAC transferred to SiO_2/Si wafer. Crease and fold at MAC edge from transfer process. **b**, Contrast-enhanced image in greyscale shows no topological features visible on MAC. **c**, Raman mapping shows that the intensity ratio of the D to G band, I_D/I_G, is uniform at the edge of transferred MAC on a Si/SiO_2 substrate. This ratio is slightly higher than the expected ratio of 0.82, as the Raman background signal is not subtracted during Raman mapping. **d**, Raman map ($50 \times 50\ \mu m^2$, with 2,500 data points) of I_D/I_G shows uniform quality over a large area (standard deviation is ±1.8%).
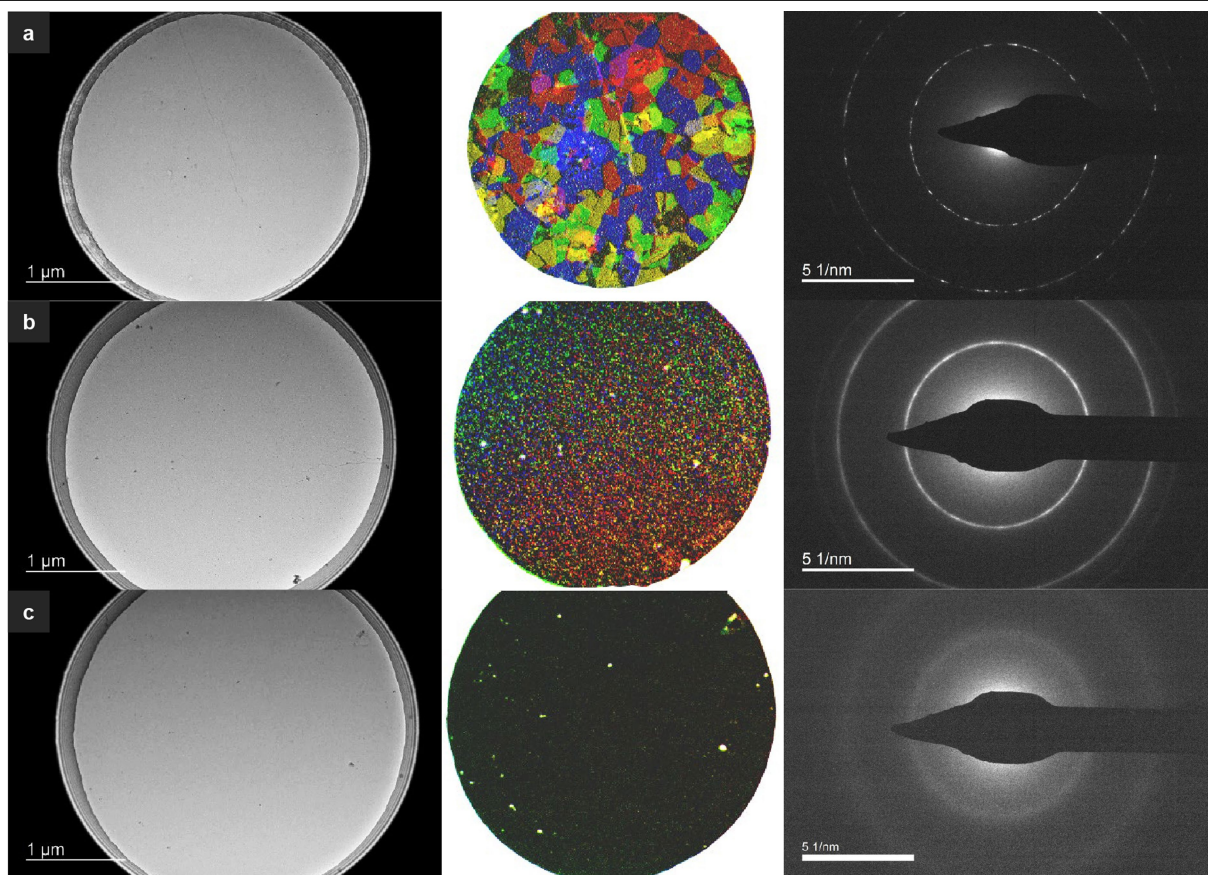
Extended Data Fig. 2 | Comparison of large-area TEM data. a, Polycrystalline graphene with grain size 200–500 nm. **b**, Nanocrystalline graphene (sample in Fig. 2i) with grain size 1–3 nm. **c**, MAC (sample in Fig. 2h). Left, bright-field TEM; centre, DF-TEM with false-colour image overlay showing crystal domains; right, SAED patterns. Both polycrystalline and nanocrystalline graphene show crystal domains under DF-TEM and have well defined SAED diffraction patterns. MAC has no visible domains in DF-TEM. Only MAC has the characteristic amorphous halo from SAED diffraction.
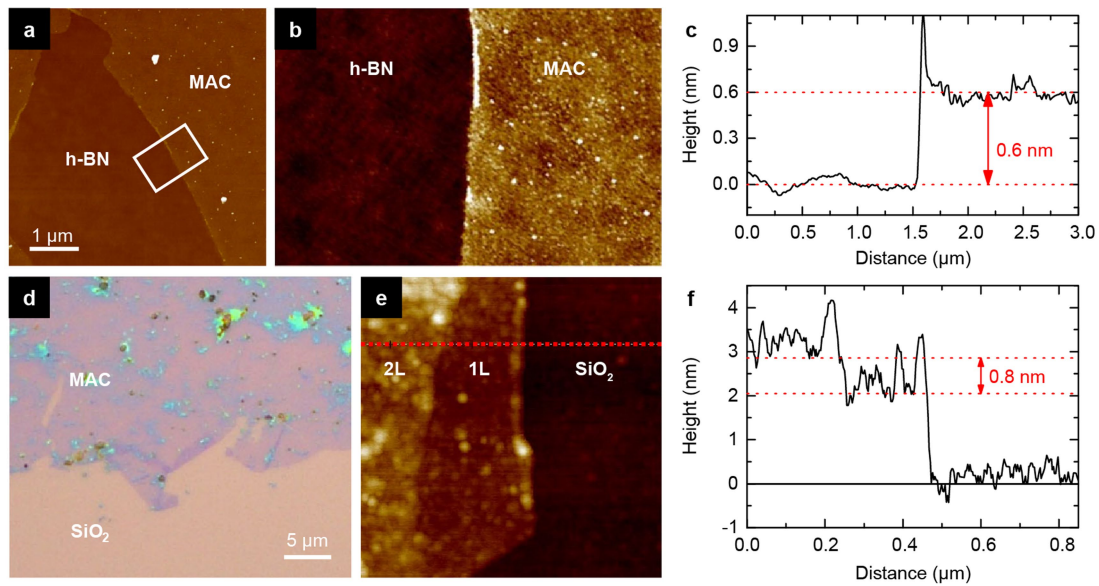
Extended Data Fig. 3 | Thickness of MAC. a, AFM topography of MAC transferred onto an atomically flat, exfoliated BN crystal. **b**, Close-up of the region indicated by the white box in **a**, with a scan length of 3 μm. **c**, Height profile of MAC, obtained by averaging vertically over the entire image scan in **b**, shows a thickness of about 0.6 nm. **d**, Optical image of MAC grown on gold substrates and transferred onto SiO_2 by wet transfer with KI/I_2 solution as gold etchant and followed by 7 h annealing in Ar/H_2 at 300 °C. For MAC transferred from gold, residues from the gold etching cannot be fully removed owing to the non-optimized transfer process. **e**, AFM topography of a folded MAC edge in **d** to obtain one and two layers. **f**, The height profile along the red dotted line in **e** gives the thickness of MAC grown on gold as about 0.8 nm. Residual contamination from the transfer step and difference in substrate interactions may account for the higher thickness of MAC when transferred from gold.
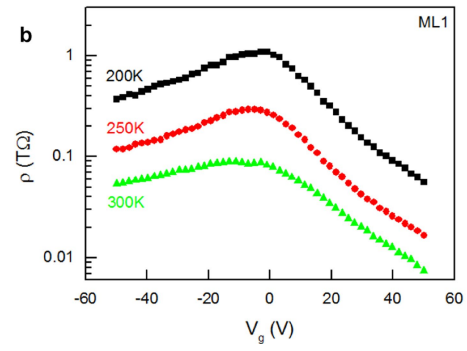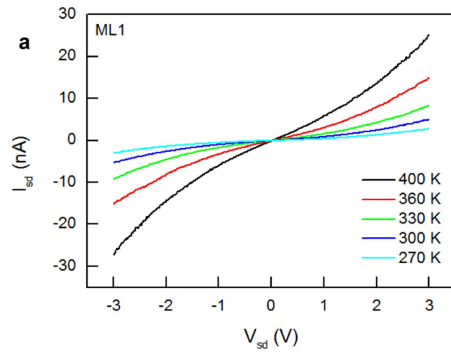
Extended Data Fig. 4 | Current–voltage measurement and gate dependence. a, Nonlinear I–V curves in Fig. 4b shown in linear scale. **b**, Gate dependence of MAC with electrostatic gating by SiO_2/Si back gate shows ambipolar behaviour and strong temperature dependence, increasing from 100 GΩ per square at room temperature to 1 TΩ per square at 200 K.
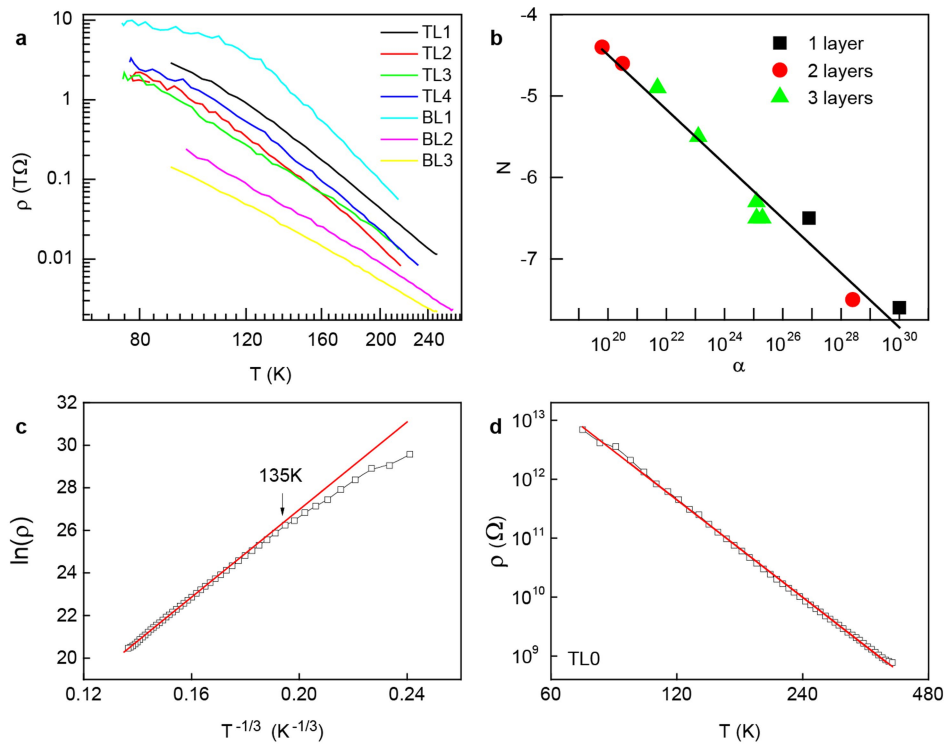
Extended Data Fig. 5 | Resistivity of samples as a function of the temperature. a, Temperature dependence of the resistivity for a set of devices with two- and three-layer MAC (denoted BL and TL, respectively). **b**, The linear fit of the resistivity of offset α and power N, as described by the formula $\rho = \alpha T^N$, shows a linear correlation, $N = 2.2(\pm 0.6) - 0.33(\pm 0.02)\log\alpha$. The data in **a**, **b** are provided in Supplementary Table. **c**, **d**, Resistivity of tri-layer MAC sample (sample ID TL0) as a function of temperature plotted in a linear scale. The Mott plot (**c**) shows a temperature limit of 135 K (indicated by the black arrow) up to which it can be applied, as opposed to a power-law dependence (**d**). The red lines are the best linear fits.
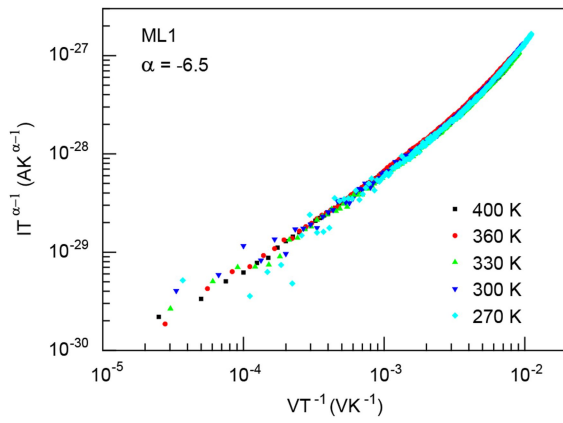
Extended Data Fig. 6 | Universal scaling of nonlinear *I–V* characteristics for ML1 sample. All *I–V* curves are collapsed to a single curve indicating apparent power-law dependence in a disordered quasi-one-dimensional system. The equation for the universal scaling curve is from ref. [21].
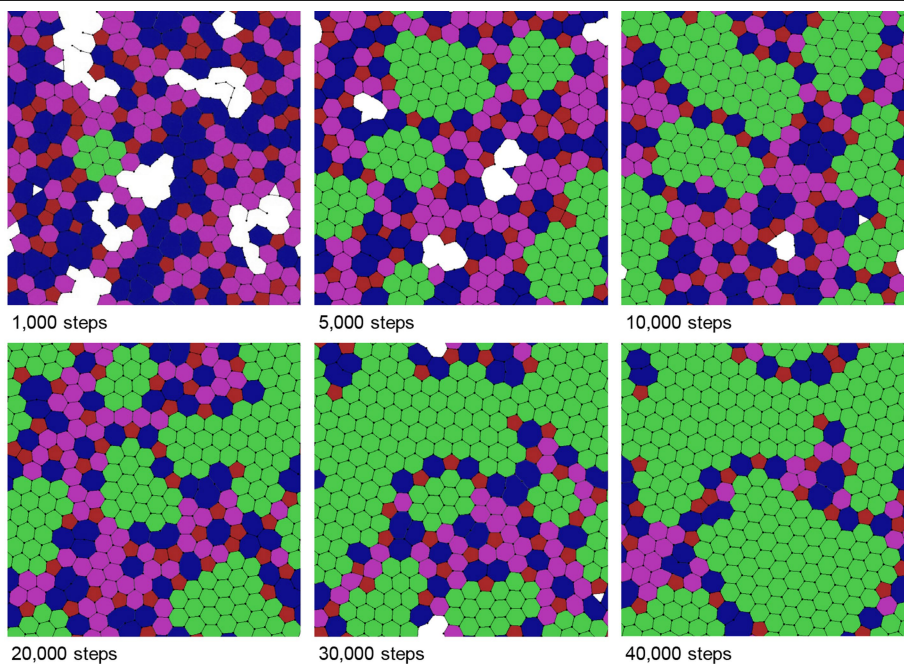
Extended Data Fig. 7 | Selection of MAC theoretical model. The configuration for the MAC structure at the 20,000th iteration is chosen as the theoretical model, shown in Fig. 2c, for its similarity to experimental HRTEM images of MAC. Previous steps also show an unstable ring structure (for example, rings with fewer than four carbon atoms, or ill-defined rings). Furthermore, the ring size distribution from 10,000 steps is similar . Colour overlay is added for identification of pentagons (red), heptagons/octagons (blue) and strained hexagons (purple or green) that are omnipresent. Crystallites (green) separate regions with non-hexagons. Crystallites are defined to consist of at least one hexagonal ring surrounded by six hexagonal rings.
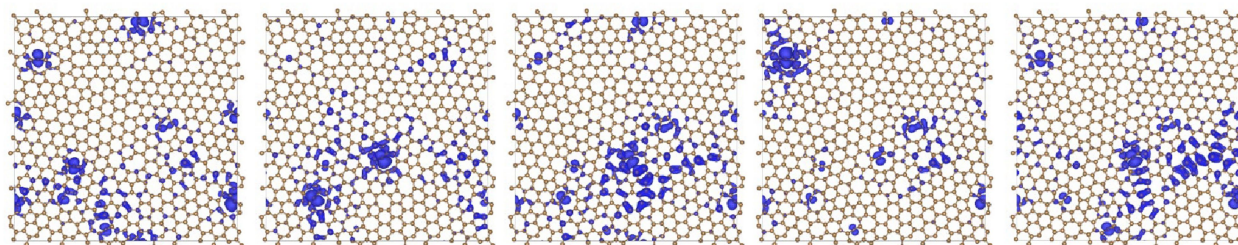
Occupied states:
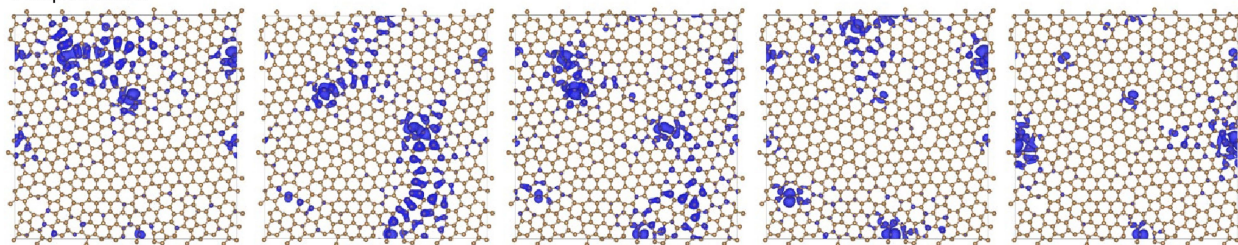
E = -0.121 eV   E = -0.10 eV   E = -0.075 eV   E = -0.028 eV   E = -0.002 eV

Empty states:

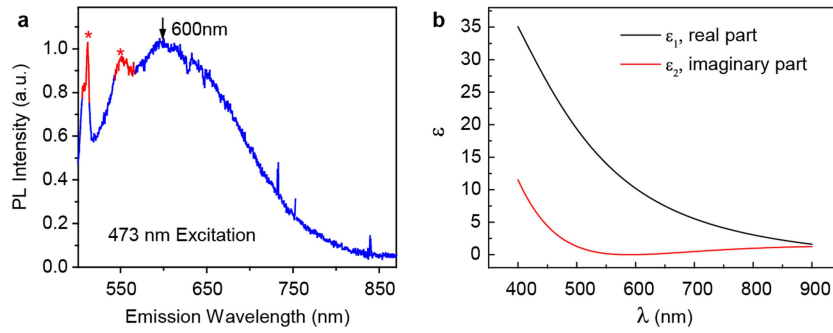E = +0.002 eV   E = +0.023 eV   E = +0.043 eV   E = +0.050 eV   E = +0.082 eV

Extended Data Fig. 8 | Modulus square of electronic wavefunctions. The lowest unoccupied wavefunctions (blue) are shown for ten states with energies closest to the Fermi energy. This shows localization on non-hexagon rings that are separated by crystallites.

Extended Data Fig. 9 | Optical measurements of MAC on SiO$_2$/Si. a, Photoluminescence spectra were measured with an excitation wavelength of 473 nm. The peaks marked by asterisks correspond to the Raman signal from MAC. The emission spectrum of the film has a broad peak centred at 600 nm. **b**, Relative permittivity of MAC on SiO$_2$/Si substrate by ellipsometry measurements. E_g is taken where the imaginary part equals zero, at about 590 nm (2.1 eV), at which the real part of the relative permittivity is approximately 11.